

VARIABILITY IN THE MECHANICAL PROPERTIES OF LASER SINTERED PA-12 COMPONENTS

M. Faes*, Y. Wang[†], P. Lava[†] and D. Moens*

* KU Leuven, Dept. of Mechanical Engineering, Technology Campus De Nayer, BE-2860 St.-Katelijne-Waver

[†] KU Leuven, Dept. of Materials Engineering, Technology Campus Ghent, BE-9000 Ghent

REVIEWED

Abstract

The quasi-static mechanical properties of Laser Sintered (LS) PA-12 material are highly influenced by the thermal history of the thermoplastic material during the production, as this impacts critical material properties such as the degree of crystallinity and porosity in the resulting component. Many process-related parameters, including preheating temperature, laser energy density, layer interaction time and post-build cooling cycle, were already shown to influence the thermal history significantly. Due to the large, mainly epistemic, variability in these parameters, the mechanical response of produced components is often difficult to predict and is moreover governed by non-isotropic constitutive equations. This work therefore focusses on the identification of this variability in the mechanical behavior and the validation of experimentally obtained non-deterministic material models. A non-deterministic (variable) constitutive model is built experimentally, based on 90 uniaxial tensile tests, performed on LS samples that were built under different orientations. This model is subsequently validated by building a well-defined benchmark sample, containing complex stress states upon loading. This sample is tested using Digital Image Correlation. Finally, a novel way of identifying non-isotropic material properties, the Virtual Fields Method, is applied to this benchmark sample to identify the constitutive parameters.

Introduction

Due to the low time-to-market, large freedom in design and efficient usage of materials and resources, Additive Manufacturing (AM) receives and increasing industrial interest, especially in sectors where weight reduction plays an important role, such as Automotive and Aerospace. An example of such an AM process that receives growing attention, is Laser Sintering (LS), as it is generally deemed to be the most robust AM process for plastics [1,2]. LS builds up complex parts based on a digital 3D - model through a layer-by-layer approach. A fine layer of polymeric powder is deposited, preheated to just below its melting temperature and selectively sintered by a laser source, binding it to previously sintered layers. After completion of the build, the material is cooled down and loose powder is removed. Thus the desired product is formed [3]. Due to the layer-by-layer nature of this process, complexity can be added to the design without increasing the cost of the production. This enables the economic production of weight optimized, tailored small series [4]. A typical lay-out of a Laser Sintering machine is shown in Figure 1. To date, different commercial machines exist, which differ in e.g. the type of laser, powder feed mechanism or means of preheating [5,6].

Due to the large complexity of parameter variations in the LS process, produced components typically show a large variability in their mechanical response. Moreover, this response is typically heterogeneous and governed by transverse isotropic or orthotropic constitutive equations on a macroscopic scale, oriented to the three principal axis of the machine, as is shown by e.g. [7–11]. In this regard, Ajoku et al (2006) found orthotropic properties in terms of Young's modulus, ranging from 1817 MPa to 2047 MPa using a 3D-Systems Vanguard LS machine [8]. Jollivet et al. (2009) found similar values using an EOS Formiga LS machine [9]. On the other hand, Amado-Becker et al (2008) employed an ultrasonic technique to determine the elastic constitutive model of PA-12 samples, identifying the samples as isotropic [10]. At last, Cooke et al. (2011) found transverse isotropy in the Young's modulus of PA-12 samples, produced with a Sinterstation HiQ platform using a statistically relevant population of 144 test samples [11].

It is generally accepted that the laser energy density and powder bed temperature are the two main factors that influence the mechanical properties of LS-PA12 components, as e.g. indicated by [12,13]. Besides, also the place

of the component in the build platform was shown to exhibit a significant effect on the Young's modulus of sintered PA12 material, due to inhomogeneities in the powder bed [6]. Other parameters that are shown to have a significant influence are e.g. the laser energy density, delay time between layers and the thermal processing window of the material [6,14]. As can be understood, aforementioned parameters directly influence the thermal history of the material during production by either impacting the temperature of the previous layer on the moment of scanning the current layer, the amount of thermal energy that is put into the current layer or the time during which the sintered material is kept above its glass transition temperature. Thus, these parameters either impact the porosity or the degree of crystallinity of the sintered component, and consequential the mechanical properties.

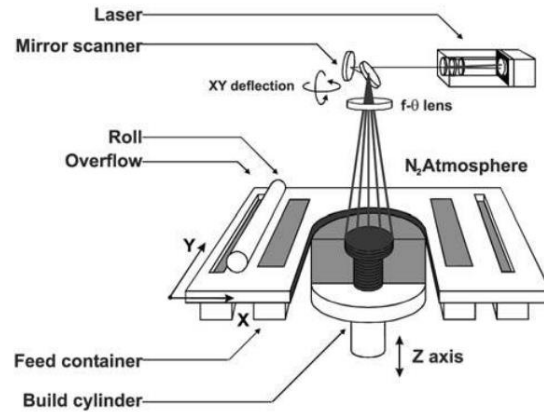


Figure 1: Typical lay-out of a Laser Sintering machine [5]

Finite Element (FE) simulations are becoming an indispensable tool in the modern engineering toolbox for designing functional components. However, the use of FE modelling for the simulation of the elastic response of LS components was only applied with limited success [15,16]. The elastic constitutive models, needed for FE simulations, are typically initiated by uniaxial testing of components which are built along the three principal axis of the machine (see e.g. [15,16]). In general, the elastic response of a material can be described by equation 1, with $\underline{\sigma}$ and $\underline{\epsilon}$ the stress and strain matrices and \underline{Q} the elastic stiffness tensor, with its various components Q_{ij} :

$$\underline{\sigma} = \underline{Q} \cdot \underline{\epsilon} \quad (1)$$

The constitutive model for a general anisotropic material is given by equation (2):

$$\begin{bmatrix} \sigma_1 \\ \sigma_2 \\ \sigma_3 \\ \sigma_4 \\ \sigma_5 \\ \sigma_6 \end{bmatrix} = \begin{bmatrix} Q_{11} & Q_{12} & Q_{13} & Q_{14} & Q_{15} & Q_{16} \\ & Q_{22} & Q_{23} & Q_{24} & Q_{25} & Q_{26} \\ & & Q_{33} & Q_{34} & Q_{35} & Q_{36} \\ & & & Q_{44} & Q_{45} & Q_{46} \\ & sym. & & & Q_{55} & Q_{56} \\ & & & & & Q_{66} \end{bmatrix} \begin{bmatrix} \epsilon_1 \\ \epsilon_2 \\ \epsilon_3 \\ \epsilon_4 \\ \epsilon_5 \\ \epsilon_6 \end{bmatrix} \quad (2)$$

Structural orthotropy is a special case of this anisotropic tensor where the coupling terms between normal stresses ($\sigma_1, \sigma_2, \sigma_3$) and shear strains ($\epsilon_4, \epsilon_5, \epsilon_6$) in the stiffness tensor are zero. The aforementioned technique for building the material model for using LS-PA12 material in FE simulations implies that the building direction is the main driving factor for the morphological properties of the material of a produced component. Moreover, it is assumed that the measured difference in Young's modulus between tensile samples, built according to these three principal directions of a LS machine is representative for all samples that are built on that machine. However, many other factors additionally influence the quasi-static properties of a LS-PA12 component, as indicated above. This research therefore aims identifying and quantifying the variability in the in-plane orthotropic properties of a LS-PA12 component. Moreover, the Virtual Fields Method is shown as a technique to determine the in-plane orthotropic properties of a component using a single test.

Methodology

Uniaxial tensile testing

Uniaxial tensile dog-bone samples (ASTM D638) are produced on a EOS P395 LS-Machine in PA2200 PA12 material with a Melt Volume Ratio (MVR) of $24.17 \text{ cm}^3/10\text{min}$ using standard commercial production parameters. A statistically significant population of 30 samples per orientation is built, resulting in a total test population of 90 samples. These samples are aligned with the three major building orientations of the machine (x,y,z) as indicated in figure 2, with z being the layering direction. A constitutive model is built under the assumption that the measured elastic mechanical properties in these directions correspond to their respective terms in the stiffness tensor. The different orientations are further denoted as ‘Upright’ for the specimen which main axis lies parallel to the z-axis, ‘Edge’ for the specimen built on its edge and ‘Flat’ for the specimen lying flat along the y-axis.

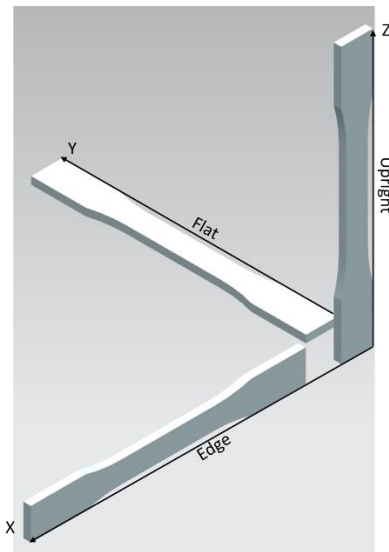


Figure 2 – Orientations along which the uniaxial samples were built

The samples are tested using an INSTRON 5900R testing machine at a strain rate of 1mm/min. The length between the grips of the machine is kept constant for all tests at 100 mm. An Instron 2620 50/5mm extensometer is used to measure the longitudinal strain ϵ_{yy} , averaged over the strain gage length of 5mm. Young’s moduli (E) are calculated by determining the slope of the stress-strain relationship of the samples of the different orientations between 0.0005 and 0.0025 strain by means of linear regression.

Additionally, Digital Image Correlation (DIC) is employed both to determine Poisson’s ratio and qualitatively measure the propagation of cracks through the specimens. Hereto, the strain fields ϵ_{xx} and ϵ_{yy} are averaged over the component under the assumption of homogeneity. DIC is a contactless full-field strain measurement technique, capable of measuring the occurring strain fields and crack propagation in loaded samples. Before the test, a random pattern is applied to the surface of the specimen using spray painting technique. During the tensile test, pictures of the specimen are taken using two 8-bit 2MP cameras, equipped with 50mm lenses on different load levels. A Zero-normalized Sum of Squared Differences matching criterion is used to track a subset of the random pattern, indicated by the subset size, across the pictures at different loading steps. This criterion was specifically chosen for its robustness with respect to both changes in picture illumination and contrast. Sub-pixel accuracy is obtained by interpolating the pictures using bicubic splines. Thus, the according deformation fields can be calculated. At last, a strain window of 15 px was used for the calculation of the strains, resulting in a Virtual Gage length of 91px. Missing data on the edges, originating from the correlation algorithm employed, is compensated for during the calculation of the displacement- and strain fields. The parameters that are used for the correlation algorithm are listed in table 1. A complete survey of these parameters can e.g. be found in [17] and [18]. The DIC measurements were made with MatchID.

Table 1 – Adopted parameters for the DIC measurements

Parameter	Value
Matching Criterion	ZNSSD
Interpolation	Bicubic Spline
Noise	0.4581 %
Pre-filtering	Gaussian
Step size	7 px
Subset size	25 px
Strain Window	15 px

Huber's equation was used to approximate the values of the shear moduli G_{ij} through the measured Young's moduli and Poisson's ratios. Huber [19] showed that G_{ij} can be approximated by:

$$G_{ij} = \frac{\sqrt{E_{ii}E_{jj}}}{2(1+\sqrt{\nu_{ij}\nu_{ji}})} \quad (3)$$

The degree of orthotropy of the different properties is calculated as:

$$O_{ij} = \frac{E_{ii}}{E_{jj}} - 1 \quad (4)$$

In order to identify the variability in the elastic properties, the distribution that best fits the measured data is selected using the Anderson-Darling distance d_{AD} [20]:

$$d_{AD} = \int_{-\infty}^{\infty} [F_n(x) - F_\theta(x)]^2 [F_\theta(x)(1 - F_\theta(x))]^{-1} dF_\theta(x) \quad (5)$$

The Anderson-Darling distance d_{AD} is a quadratic type distance between the empirical distribution function $F_n(x)$ and the hypothesized distribution function $F_\theta(x)$, where more weight is given to the tails of the distribution as compared with the Kolmogorov-Smirnov test. This is relevant for identification of distributions for use in reliability estimation. Numerically, this yields:

$$d_{AD} = -n - \sum_{i=1}^n \frac{2i-1}{n} [\ln(F_\theta(x_i)) + \ln(1 - F_\theta(x_{n+1-i}))] \quad (6)$$

Where $\{x_1, x_2, \dots, x_n\}$ are the ordered n sample data points. The hypothesized distribution exhibiting the lowest Anderson-Darling distance is selected to be the best fitting distribution. In this regard, it is tested how the statistical distribution of aforementioned parameters can be explained using a Normal, Lognormal, Weibull or Gamma distribution. The candidate distribution will only be accepted if the corresponding p-value is larger than the chosen threshold of 0.05.

Determination of material properties using the Virtual Fields Method

In order to validate the built constitutive model, the Virtual Fields Method is employed to alternatively determine the elastic constitutive parameters. The Virtual Fields method, as introduced by Grédiac and Pierron (2012), is a numerical technique to determine the elastic stiffness tensor \underline{Q} , based on a measurement of the strain field ϵ and the load \bar{T} in a loaded component, regarded over the length L_f . [21]. Based on the Virtual Work principle, formula (5) can be derived for the orthotropic case under plane-stress assumption (see [21]):

$$\int_{S_v} Q_{11} \epsilon_1 \epsilon_1^* dS + \int_{S_v} Q_{22} \epsilon_2 \epsilon_2^* dS + \int_{S_v} Q_{12} (\epsilon_1 \epsilon_2^* + \epsilon_2 \epsilon_1^*) dS + \int_{S_v} Q_{66} \epsilon_6 \epsilon_6^* dS = \int_{L_f} \bar{T}_i u_i^* dl \quad \forall u^* \in KA \quad (7)$$

Herein, Q_{ij} are the in-plane constitutive parameters of the orthotropic material model, as presented in equation (2), ϵ_i are the measured strain fields in all the in-plane directions, u_i the measured displacement field and \bar{T}_i the measured force on the specimen. S_v is the surface of the component over which the strain fields are measured. The parameters indicated by * are virtual fields. This formula is valid for any kinematically admissible virtual displacement field. Choice of as many independent virtual fields as unknown Q_{ij} leads to a set of equations which yields the constitutive model of the material. The engineering constants of the material (E_i , ν_{ij} and G_{ij}) at last are calculated from these Q_{ij} . Specifically for this purpose, a test geometry was defined which induces a bi-axial stress state upon uniaxial loading. This geometry is shown in figure 3. In this way, all constitutive parameters of the material model for plane-stress are activated and can thus be measured through the VFM method. For each orientation ('Edge', 'Flat' and 'Upright'), four samples are built and tested using DIC. The constitutive model parameters are determined using the VFM. To validate the material model, built by the uniaxial tests, the identified distributions are compared with the material models that were built by the VFM.

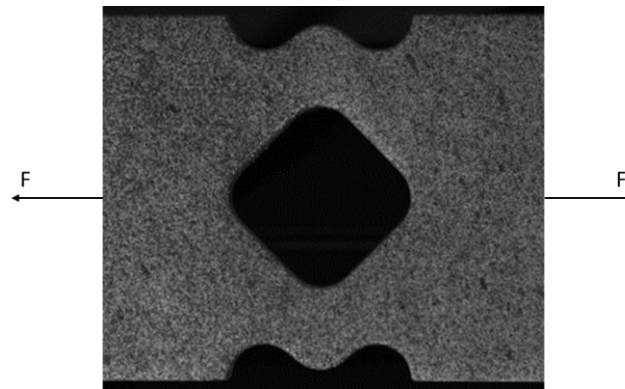


Figure 3 – Bi-axial testing geometry

Results and Discussion

Uniaxial tensile testing

Table 2 shows the measured quasi-static elastic properties of the tested LS-PA12 components and their variability. The Young's modulus, averaged over the 90 specimens was measured to be 1653 MPa with a coefficient of variance (COV) of 5.0%. Poisson's coefficient was measured to be 0.3967 with a COV of 1.9%. As can be noted, the measured COV on Young's modulus is large (5%), when all the measured samples are considered. Therefore, the use of deterministic FE simulations in the design of an LS-PA12 component, while neglecting the effect of the production process on the quasi-static properties could result in a severe bias with respect to the actual mechanical behavior of the produced part. Therefore, a more reliable way of designing these components, is by incorporating this variability already in a design phase.

Table 2 – Variability in the mechanical properties of the LS samples

	Nominal	St. Dev.	COV
E_{11} [MPa]	1653	114.89	5.0%
ν_{12} [/]	0.3967	0.0075	1.9%

Table 3 shows the measured material properties, grouped by the respective orientations. Young's modulus for the 'Edge', 'Upright' and 'Flat' orientations is measured to be 1620 MPa, 1660 MPa and 1680 MP respectively with a respective COV of 5.61%, 6.5% and 5.83%. Poisson's ratio for 'Edge', 'Upright' and 'Flat' orientations is found to be 0.3937, 0.3871 and 0.4093 respectively with a maximum COV of 1.63% for the Flat direction. The shear moduli are calculated to be 588.58 MPa, and 586.48MPa 600.54 MPa respectively. The variability on the shear modulus is omitted as this value is calculated from the measured Young's modulus and Poisson's ratio

using equation (3). The degree of orthotropy between the different orientations is relatively low, with a maximum of 3.57% between the ‘Edge’ and ‘Flat’ direction.

Therefore, following these results, the elastic mechanical response of LS-PA12 can be assumed to have quasi-isotropic constitutive parameters.

Table 3 – Material properties per orientation, as obtained by uniaxial testing. The * indicates that the variable was calculated.

	Upright	St. Dev.	COV	Edge	St. Dev.	COV	Flat	St. Dev.	COV
E_{ii} [MPa]	1660	108	6.5%	1620	91	5.61%	1680	98	5.83%
ν_{ij} [/]	0.3937	0.0034	0.86%	0.3871	0.0008	0.21%	0.4093	0.0067	1.63%
G_{ij}^* [MPa]	586.48	/		588.58	/		600.54	/	
O_{ij}^* [%]	2.46			-3.57			1.2%		

Typical stress-strain relationships for the tested samples are shown in figure 4. The DIC measurement are shown corresponding with the respective place on the stress-strain curve of the test. No distinct difference between the ‘Edge’ and ‘Flat’ specimens is evident from these plots in terms of the introduction and propagation of the failure in the specimen. On the other hand, failure in the ‘Upright’ sample is initiated at the side of the specimen and further propagates towards the middle. Besides, it can be noted that failure in the ‘Upright’ samples occurs at lower stress and strain levels, as compared to the other two directions. This can be explained by the fact that the failure in an ‘Upright’ sample stems from the separation of two successive layers, due to inter-layer porosity [2]. On the other hand, for the ‘Edge’ and ‘Flat’ orientations, this failure is formed perpendicular with the layering direction and results in a wedge-like failure.

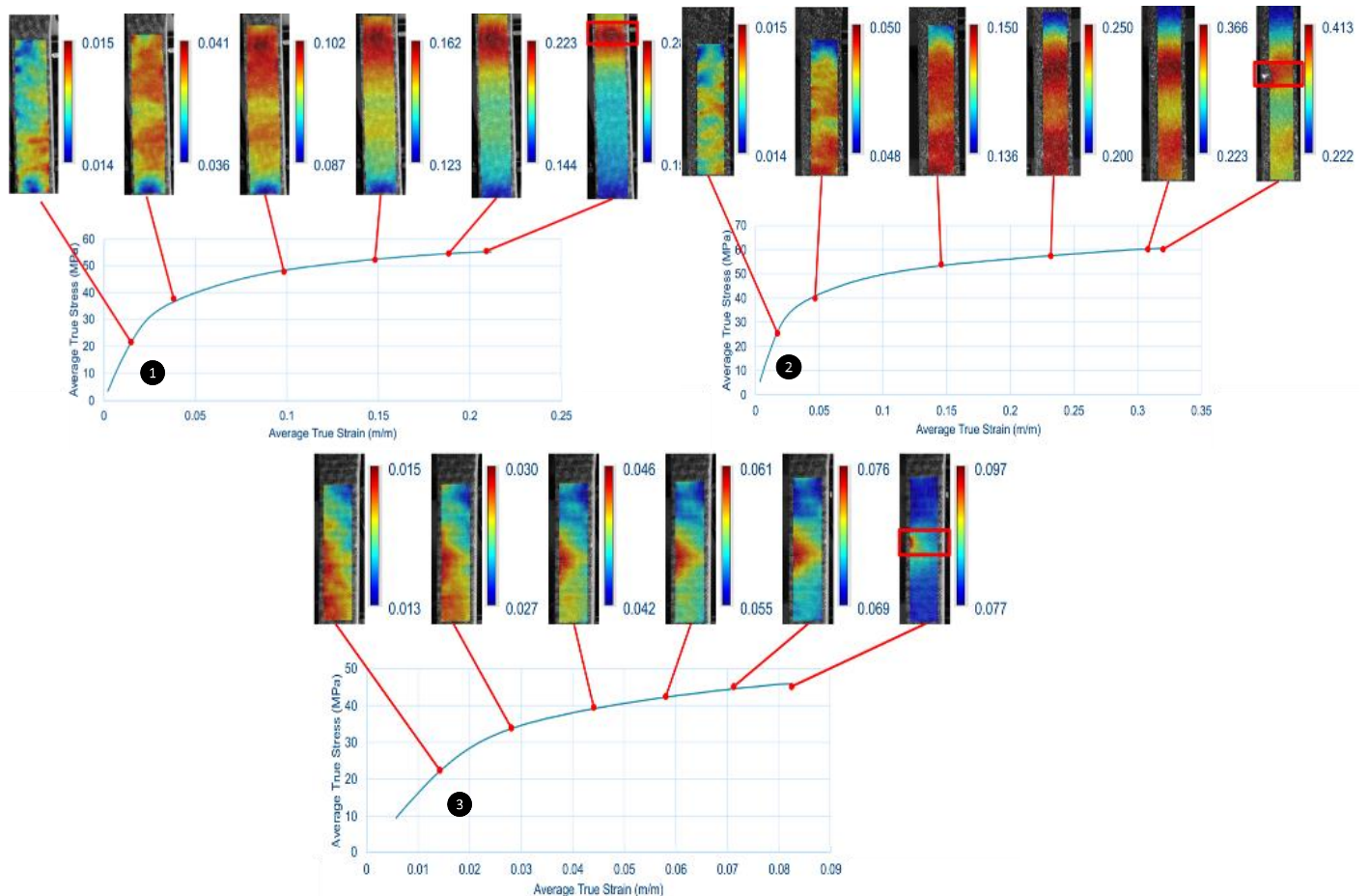


Figure 4 – Stress-Strain relationship for an ‘Edge’ (1), ‘Flat’(2) and ‘Upright’ (3) specimen with the corresponding strain fields at several load steps

Table 4 shows the calculated Anderson-Darling distances when respectively a Normal, Lognormal, Weibull and a Gamma distribution is fitted to the Young’s modulus data. As is evident, the lowest AD-distance can be achieved with a Normal distribution fitted to the data of all the different orientations separately, as combined into a single population (pooled). It should however be noted that the p-value of the calculated AD distances for the ‘Flat’ orientation is lower than the limit of 0.05, due to multi-modality in the data. Therefore, these results should be interpreted with care. The mean and standard deviation of these can be found in table 2 and table 3.

Hence, it is possible to account for the variability in Young’s modulus without prior knowledge on the process in a design simulation by taking this identified distribution into account.

Table 4 – Anderson-Darling distances of the selected distributions for the 90 samples (pooled) and the different orientations

Distribution	Pooled		Edge		Flat		Upright	
	AD	p	AD	p	AD	p	AD	p
Normal	0.266	0.68	0.350	0.37	0.794	0.03	0.776	0.36
Lognormal	0.327	0.51	0.360	0.41	0.777	0.04	0.785	0.34
Weibull	0.580	0.14	0.849	0.02	0.909	0.02	0.820	0.29
Gamma	0.305	0.25	0.391	0.25	0.834	0.03	0.840	0.23

Closer inspection of the DIC measurements shows heterogeneities in the strain fields of a loaded tensile bar, where this cannot be explained through the loading condition, as indicated in figure 5. These samples show locally higher strains of 5 – 10% in a repetitive stripe pattern, indicating a local lower stiffness of the material at these locations. The physical phenomena behind this pattern yet remain unknown.

It can as well be noted that a local higher strain exists in the sample throughout the test, as indicated by the red band in the middle of the specimen. Also, yielding was initiated at that exact location. This location in the specimen corresponds to those layers in the ‘Upright’ sample where an ‘Edge’ sample was built at the same time. This is also shown in figure 5. This results an increase in scanning of these layers, permitting the sintered layer of material to cool further down as compared to layers in the ‘Upright’ specimen where the ‘Edge’ part is not present. This decrease in temperature in its turn disadvantages the sintering conditions for the next layer, leading to a lack of connection between the layers and thus a locally lower stiffness. Therefore, it is assumed that other samples in the build significantly influence the local properties of LS-PA12 material. This assumption will be validated in further research by combining these results with XCT measurements, performed on the samples.

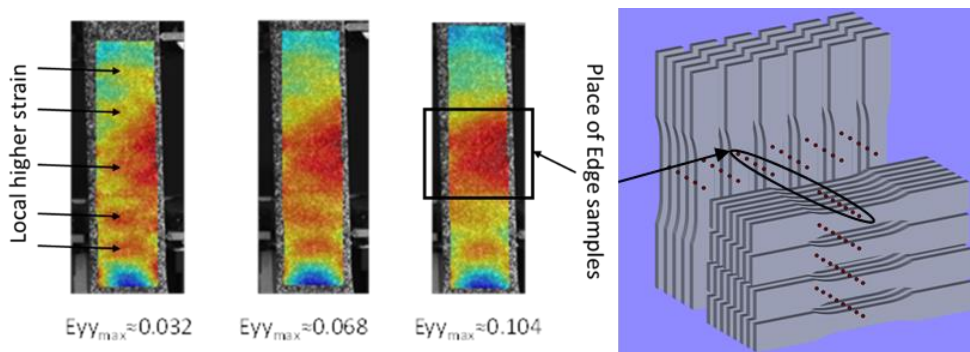


Figure 5 – Heterogeneous strain profile in upright built LS samples with a cross section of the placement of upright and edge specimens in the build volume

Determination of material properties using the Virtual Fields Method

The strain fields in the transverse (ϵ_{xx}), longitudinal (ϵ_{yy}) and shear (ϵ_{xy}) in an ‘Upright’ built bi-axial sample at a load level of 3250N are shown in figure 6. As is evident from these plots, a bi-axial strain state is induced in the geometry. This strain state ‘activates’ all in-plane constitutive parameters, hence permitting the identification of this constitutive model using the VFM.

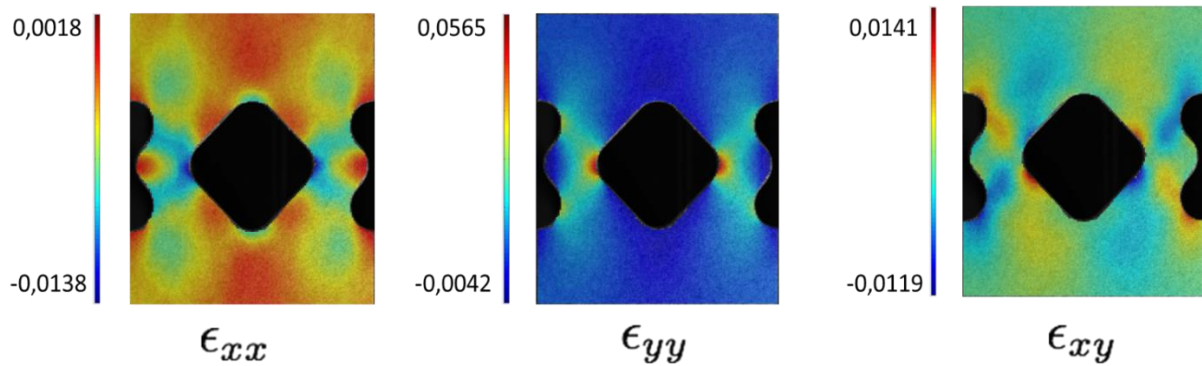


Figure 6 – Measured strain fields in the transverse (ϵ_{xx}), longitudinal (ϵ_{yy}) and shear (ϵ_{xy}) in the bi-axial test sample at a load of 3250N

The results of the Virtual Fields method calculations are shown in table 5. For the ‘Upright’ sample, The primary Young’s moduli (E_{11}) and shear moduli (G_{12}) are found to be slightly lower as compared to the results obtained by the uniaxial testing. Poisson’s coefficients however correspond well.

Moreover, these results show quasi-isotropic constitutive parameters, with a maximum O_{12} of 8.68% for the Edge direction. This confirms the quasi-isotropic assumption that was made based on the uniaxial testing. Also Poisson’s ratio and the Shear moduli are consistent for all tested orientations, further strengthening this assumption. The COV on the test results of this test population is smaller compared to the COV of those, determined by uniaxial testing with a maximum COV of 5.37% for Young’s modulus, 2.43% for Poisson’s ratio and 8.23% for the Shear modulus. However, this can be attributed to the rather small test population of 4 replica that was used for the VFM. Moreover, the biaxial parts all were located in the center of the build, whereas some replica of the uniaxial samples were more located at the edges of the machine. The bi-axial parts thus had less influence from powder bed temperature inhomogeneities.

Table 5 – Material properties, as obtained by the VFM

	Upright	St. Dev.	COV	Edge	St. Dev.	COV	Flat	St. Dev.	COV
E_{11} [MPa]	1596.67	66.58	5.37%	1550.00	61.91	4.11%	1575.00	33.17	2.11%
E_{22} [MPa]	1626.67	75.06	4.62%	1697.50	36.97	2.27%	1667.50	65.51	3.92%
ν_{12} [/]	0.41	0.01	2.43%	0.41	0.01	2.43%	0.42	0.01	2.38%
G_{12} [MPa]	545.33	37.90	8.23%	545.50	29.26	5.46%	544.50	14.15	2.60%
O_{12}^* [%]	-1.84			-8.68			-5.55		

When the measurements of Young’s moduli of the samples under the different orientations (‘Edge’, ‘Flat’ and ‘Upright’) are analyzed with respect to the principle axis of the machine, the quasi static assumption is affirmed, as can be seen in table 6. This analysis shows Young’s moduli of respectively 1583.89 MPa, 1667.5 MPa and 1647.08 MPa for the X, Y and Z axis of the employed machine. A student-t test with a confidence level α of 0.05 indeed shows that the orientation doesn’t have a significant effect on the Young’s modulus of the LS-PA12 samples. Combined into one Young’s Modulus for the LS-PA12 material, this yields 1632.82 MPa with a standard deviation of 74.31 MPa. Analogously, Poisson’s ratio and the shear modulus were found to be 0.41 and 545.2 MPa respectively.

Table 6 – Young’s moduli, as obtained by the VFM, order by the principal axis of the LS machine

	Upright	St. Dev.	Edge	St. Dev.	Flat	St. Dev.	Combined	St. Dev.
X [MPa]	1626.67	66.58	1550.00	63.77	1575.00	33.17	1583.89	68.10
Y [MPa]	/	/	/	/	1667.50	65.51	1667.5	65.51
Z [MPa]	1596.67	66.58	1697.50	59.09	/	/	1647.08	55.47
							1632.82	74.31

It can be noted that the Young's moduli, obtained through the VFM are found to be slightly lower as compared to the uniaxial tensile tests. This can be explained through the heterogeneity of the LS-PA12 component, as also indicated in figure 5. In comparison to conventional techniques, where Young's modulus calculation is based on strain values, obtained by dividing the elongation of the component by the gage length, VFM uses the full-field DIC strain data. Therefore, local heterogeneities impact the calculation of the constitutive parameters more significantly. On the other hand, also the LS process itself can affect these properties. Due to the different geometry of the bi-axial and uniaxial samples, the thermal history will differ as well. Moreover, the topology of both builds was different, further influencing this difference in thermal history.

Conclusion

This paper describes an experimental investigation to determine the variability in the mechanical properties of LS-PA12 material, built along the principal axis of the machine. Specifically, the elastic constitutive model of the material, including Young's modulus, Poisson's coefficient and the shear modulus were investigated using uniaxial tensile tests and Digital Image Correlation. Additionally, the Virtual Fields Method was employed to determine the in-plane constitutive parameters of LS-PA12 material.

The variability in the aforementioned quasi-static properties was investigated by performing 30 tensile tests for each axis of the machine, resulting in a population of 90 specimens. A rather large COV was found in Young's moduli (5%) and Poisson's coefficient (1.9%) of all the produced samples combined. Regarding the different orientations, a COV of 6.5%, 5.61% and 5.83% for respectively the 'Upright', 'Edge' and 'Flat' samples was found. Therefore, the use of deterministic FE simulations in the design of a LS-PA12 component, while neglecting this variability on the quasi-static properties could result in a severe bias with respect to the actual mechanical behavior of the produced part. For this reason, the use of non-deterministic FE models, which incorporate this variability, is encouraged for the design of functional LS-PA12 components.

The difference in fracture behavior between 'Edge', 'Flat' and 'Upright' built specimens was investigated, using DIC. No distinct difference in failure between the 'Edge' and 'Flat' orientations was found. The 'Upright' sample on the other hand failed due to inter-layer porosities. These specimens show a crack initiation at the side, stemming from the separation of subsequent layers.

It was found that the simultaneous production of parts, loaded in the layering direction, can severely affect the local stiffness properties of this part. This is attributed to the increased scanning time of a layer, by introducing extra parts, which in its turn affects the local porosity of the specimen. Further work will combine X-ray Computer Tomographical measurements with DIC to further investigate this heterogeneity.

Finally, the Virtual Fields Method was applied to a bi-axial test geometry to calculate the in-plane orthotropic constitutive parameters of the built specimens. This method was shown to deliver accurate measurements. A slight discrepancy between the uniaxial and bi-axial tests was noted and attributed to the difference in thermal history between the different samples. Thermal monitoring however is needed to validate this assumption.

Thus, a quasi-isotropic constitutive model with a Young's modulus of 1613,2 MPa, shear modulus of 540.2 MPa and a Poisson's coefficient of 0.41 could be identified by combining the VFM calculations on the specimens that were according to the considered orientations.

Acknowledgement

The authors would like to acknowledge the Agency for Innovation by Science and Technology in Flanders (IWT) for the funding in the framework of the TETRA project 130211 "AMPLIFY", Additive Manufacturing of Polymers: Innovating Functionality through reliability.

The authors would also like to acknowledge dr. T. Craeghs and M. Pavan of Materialise NV for the production of the test samples and interesting discussion of the results.

Bibliography

- [1] T. Wohlers, T. Caffrey, Wohlers Report, Wohlers Associates, Fort Collins, 2014.
- [2] D.K. Leigh, D.L. Bourell, J.J. Beaman Jr, Effect of In-Plane Voiding on the Fracture Behavior of Laser Sintered Polyamide, Scanning Electron Microscopy. (2011) 453–463. doi:10.1115/ISFA2012-7102.
- [3] H.L. Marcus, J.W. Barlow, J.J. Beaman, D.L. Bourell, From computer to component in 15 minutes: The integrated manufacture of three-dimensional objects, JOM. 42 (1990) 8–10. doi:10.1007/BF03220915.

- [4] P. Reeves, C. Tuck, R. Hague, Additive Manufacturing for Mass Customization, in: F.S. Fogliatto, G.J.C. da Silveira (Eds.), *Mass Customization Engineering and Managing Global Operations*, Springer London, London, 2011: pp. 275–290. doi:10.1007/978-1-84996-489-0.
- [5] J.-P. Kruth, P. Mercelis, J. Van Vaerenbergh, L. Froyen, M. Rombouts, Binding mechanisms in selective laser sintering and selective laser melting, *Rapid Prototyping Journal*. 11 (2005) 26–36. doi:10.1108/13552540510573365.
- [6] R.D. Goodridge, C.J. Tuck, R.J.M. Hague, Laser sintering of polyamides and other polymers, *Progress in Materials Science*. 57 (2012) 229–267. doi:10.1016/j.pmatsci.2011.04.001.
- [7] U. Ajoku, N. Hopkinson, M. Caine, Experimental measurement and finite element modelling of the compressive properties of laser sintered Nylon-12, *Materials Science and Engineering: A*. 428 (2006) 211–216. doi:10.1016/j.msea.2006.05.019.
- [8] U. Ajoku, N. Saleh, N. Hopkinson, R.J.M. Hague, P. Erasenthiran, Investigating mechanical anisotropy and end-of-vector effect in laser-sintered nylon parts, *Proceedings of the Institution of Mechanical Engineers, Part B: Journal of Engineering Manufacture*. 220 (2006) 1077 – 1086.
- [9] T. Jollivet, a. Darfeuille, B. Verquin, S. Pillot, Rapid manufacturing of polymer parts by selective laser sintering, *International Journal of Material Forming*. 2 (2009) 697–700. doi:10.1007/s12289-009-0604-8.
- [10] A. Amado-Becker, J. Ramos-Grez, M.J. Yañez, Y. Vargas, L. Gaete, Elastic tensor stiffness coefficients for SLS Nylon 12 under different degrees of densification as measured by ultrasonic technique, *Rapid Prototyping Journal*. 14 (2008) 260–270. doi:10.1108/13552540810907929.
- [11] W. Cooke, R.A. Tomlinson, R. Burguete, D. Johns, G. Vanard, Anisotropy, homogeneity and ageing in an SLS polymer, *Rapid Prototyping Journal*. 17 (2011) 269–279. doi:10.1108/13552541111138397.
- [12] Y. Guo, K. Jiang, D.L. Bourell, Accuracy and mechanical property analysis of LPA12 parts fabricated by laser sintering, 42 (2015) 175–180.
- [13] B. Caulfield, P.E.E. McHugh, S. Lohfeld, Dependence of mechanical properties of polyamide components on build parameters in the SLS process, *Journal of Materials Processing Technology*. 182 (2007) 477–488. doi:10.1016/j.jmatprotec.2006.09.007.
- [14] J.D. Williams, C.R. Deckard, Advances in modeling the effects of selected parameters on the SLS process, *Rapid Prototyping Journal*. 4 (1998) 90–100. doi:10.1108/13552549810210257.
- [15] S. Cahill, S. Lohfeld, P.E. McHugh, Finite element predictions compared to experimental results for the effective modulus of bone tissue engineering scaffolds fabricated by selective laser sintering., *Journal of Materials Science. Materials in Medicine*. 20 (2009) 1255–62. doi:10.1007/s10856-009-3693-5.
- [16] W. Cooke, R.A. Tomlinson, R. Burguete, D. Johns, G. Vanard, C. Featherston, Using Selective Laser Sintering to produce Scaled Structural Models, in: *Proceedings of the SEM Annual Conference*, Albuquerque New Mexico, 2009.
- [17] P. Lava, S. Cooreman, S. Coppieters, M. De Strycker, D. Debruyne, Assessment of measuring errors in DIC using deformation fields generated by plastic FEA, *Optics and Lasers in Engineering*. 47 (2009) 747–753. doi:10.1016/j.optlaseng.2009.03.007.
- [18] Y. Wang, P. Lava, S. Coppieters, M. De Strycker, P. Van Houtte, D. Debruyne, Investigation of the uncertainty of DIC under heterogeneous strain states with numerical tests, *Strain*. 48 (2012) 453–462. doi:10.1111/j.1475-1305.2012.00840.x.
- [19] M.T. Huber, The theory of crosswise reinforced ferroconcrete slabs and its application to various constructional problems involving rectangular slabs, *Der Bauingenieur*. 4 (1923) 354–360.
- [20] M.A. Stephens, EDF Statistics for Goodness of Fit and Some Comparisons, *Journal of the American Statistical Association*. 69 (1974) 730–737. doi:10.1080/01621459.1974.10480196.
- [21] F. Pierron, M. Grédiac, *The Virtual Fields Method*, Springer New York, New York, NY, 2012. doi:10.1007/978-1-4614-1824-5.